Research Article | Vol. 10, No. 6 | 1 May 2019 | BIOMEDICAL OPTICS EXPRESS 2719
Biomedical Optics EXPRESS

In vivo longitudinal depth-wise visualization of tumorigenesis by needle-shaped side-view confocal endomicroscopy

JINHYO AHN,[1,2,6] EUNJI KONG,[3,6] KIBAEK CHOE,[1,2] EUNJOO SONG,[1,2] YOONHA HWANG,[1,2] HOWON SEO,[1,2] INWON PARK,[2,4,5] AND PILHAN KIM[1,2,3,4,*]

[1]*Graduate School of Nanoscience and Technology, Korea Advanced Institute of Science and Technology (KAIST), 291 Deahak-ro, Yuseong-gu, Daejeon, 34141, South Korea*
[2]*KI for Health Science and Technology (KIHST), Korea Advanced Institute of Science and Technology (KAIST), 291 Deahak-ro, Yuseong-gu, Daejeon, 34141, South Korea*
[3]*Biomedical Science and Engineering Interdisciplinary Program, Korea Advanced Institute of Science and Technology (KAIST), 291 Deahak-ro, Yuseong-gu, Daejeon, 34141, South Korea*
[4]*Graduate School of Medical Science and Engineering, Korea Advanced Institute of Science and Technology (KAIST), 291 Deahak-ro, Yuseong-gu, Daejeon, 34141, South Korea*
[5]*Department of Emergency Medicine, Seoul National University Bundang Hospital (SNUBH), 82, Gumi-ro 173 Beon-gil, Bundang-gu, Seongnam-si, Gyeonggi-do, 13620, South Korea*
[6]*These authors contributed equally*
[*]*pilhan.kim@kaist.ac.kr*

Abstract: *In vivo*, longitudinal observation of tumorigenesis in a live mouse model over an extended time period has been actively pursued to obtain a better understanding of the cellular and molecular mechanism in a highly complex tumor microenvironment. However, common intravital imaging approaches based on a conventional laser scanning confocal or a two-photon microscope have been mostly limited to the observation of superficial parts of the solid tumor tissue. In this work, we implemented a small diameter needle-shaped side-view confocal endomicroscope that can be directly inserted into a solid tumor in a minimally-invasive manner *in vivo*. By inserting the side-view endomicroscope into the breast tumor from the surface, we achieved *in vivo* depth-wise cellular-level visualization of microvasculature and fluorescently labeled tumor cells located deeply inside the tumor. In addition, we successfully performed longitudinal depth-wise visualization of a growing breast tumor over three weeks in a live mouse model, which revealed dynamic changes in microvasculature such as a decreasing amount of intratumoral blood vessels over time.

1. Introduction

Tumor microenvironments are constituted by not only tumor cells but also numerous stromal cells and immune cells with blood vessels and various soluble factors such as hypoxia-inducible factors. In the development of a tumor, called tumorigenesis, not only tumor cell but also diverse types of cells including immune, vascular and stromal cells interact with each other in a highly complex and dynamic manner at the cellular and molecular level [1–8]. It is imperative to improve our understanding of the tumor microenvironment to develop a more effective target therapy and optimize treatment strategies. Direct *in vivo* observation of cellular-level phenomena inside tumor tissue is highly desirable as it can provide new insight into the complex and dynamic processes in tumorigenesis [9–15]. In addition, to observe the single tumor-bearing mouse over an extended period of time, several imaging window techniques have been developed for various organs and tissues such as subcutaneous tissue [16,17], brain [18], mammary fat pad [19], intestine [20], and liver [21]. However, high-resolution intravital imaging has been mostly limited to the superficial portion of the tumor

#361204 https://doi.org/10.1364/BOE.10.002719
Journal © 2019 Received 28 Feb 2019; revised 24 Apr 2019; accepted 28 Apr 2019; published 7 May 2019

tissues. This is mainly due to a rapidly deteriorating signal-to-background ratio in the image acquired at a deeper portion of tissues, which is mainly caused by increased multiple light scattering. To overcome this limitation, a miniature optical probe based on graded-index (GRIN) rod lenses was suggested to enable cellular-level deep tissue imaging [22–29]. However, a longitudinal *in vivo* cellular-level visualization of deep tumor tissue during tumorigenesis to investigate the dynamically changing microenvironment and complex pathophysiology has remained as a challenging task.

In this study, by utilizing GRIN lenses based side-view endomicroscope integrated into a small-diameter needle, we successfully achieved minimally-invasive cellular-level depth-wise visualization of microvasculature and fluorescently labeled tumor cells deeply placed inside a solid tumor. The side-view endomicroscope was fabricated by attaching 350 μm diameter triplet GRIN lenses consisting of a coupling lens, a relay lens, and an imaging lens with an aluminum coated 90° micro-prism. It was then packaged into a commercial hypodermal 22 gauge needle tip for direct and stable insertion to the deep region of solid tissue in a live mouse. To demonstrate the depth-wise imaging performance of the side-view endomicroscope into the deep tissue, it was inserted into the dorsal skin layer of a H2B-GFP transgenic mouse in which fluorescent nuclei were successfully visualized from the epidermis to the deeper dermis and microvasculature simultaneously. Finally, we successfully performed repetitive and longitudinal depth-wise visualization of a growing tumor in the orthotropic mouse model of breast cancer during three weeks, which revealed dynamic changes in microvasculature such as a decrease of intratumoral blood vessels over the time-course of tumorigenesis.

2. Materials and methods

2.1 Needle-shaped side-view endomicroscope based on GRIN lens

A side-view endomicroscope was fabricated based on miniature GRIN lenses, as shown in Fig. 1(a). It consists of a high NA coupling lens (NA: 0.5), a 1.5 pitch relay lens (NA: 0.2), and an imaging lens (NA: 0.43) with a diameter of 350 μm attached to a 90° micro-prism (base length: 300 μm) with a reflective aluminum coating on the hypotenuse surface to reflect light for side-viewing. The working distance of the coupling lens is 100 μm when the focal point made by imaging lens is on the surface of the micro-prism. The fabricated side-view endomicroscope with a total length of 13.7 mm was packaged into a hypodermal 22 gauge needle tip (PrecisionGlide syringe needle, BD) by using a UV curing optical adhesive (NOA61, Norland Products). The NA of the imaging lens was calculated by ray-tracing software, which was polished to achieve the working distance of 100 μm for coupling lens when the focal point made by the imaging lens is on the surface of attached micro-prism. The fabricated optics with total length of 13.7 mm and diameter of 350 μm was packaged into a hypodermal 22 gauge needle tip (PrecisionGlide syringe needle, BD) with the nominal inner diameter of 0.41 mm using a UV curing optical adhesive (NOA61, Norland Products). To avoid excessive damage to the tissue and to protect the micro-prism, the empty space between the needle tip and the prism was filled with a UV-curing adhesive. The finally packaged needle-shaped side-view endomicroscope had a diameter of 0.7 mm and a length of 15.4 mm. As shown in Fig. 1(b), for *in vivo* deep tissue imaging with an anesthetized mouse, the side-view endomicroscope was fixed to a custom-design mount consisting of XY translation mount (CXY1, Thorlabs) and Z-axis translation stages (9061-COM-M, Newport) for precise adjustment of the position under the objective lens. After integration into the imaging system, the needle-shaped side-view endomicroscope with the magnification of 0.83 provided a circular-shaped field of view (FOV) with diameter of 180 μm and transverse and axial resolutions of about 1 and 10 μm, respectively.

Biomedical Optics EXPRESS

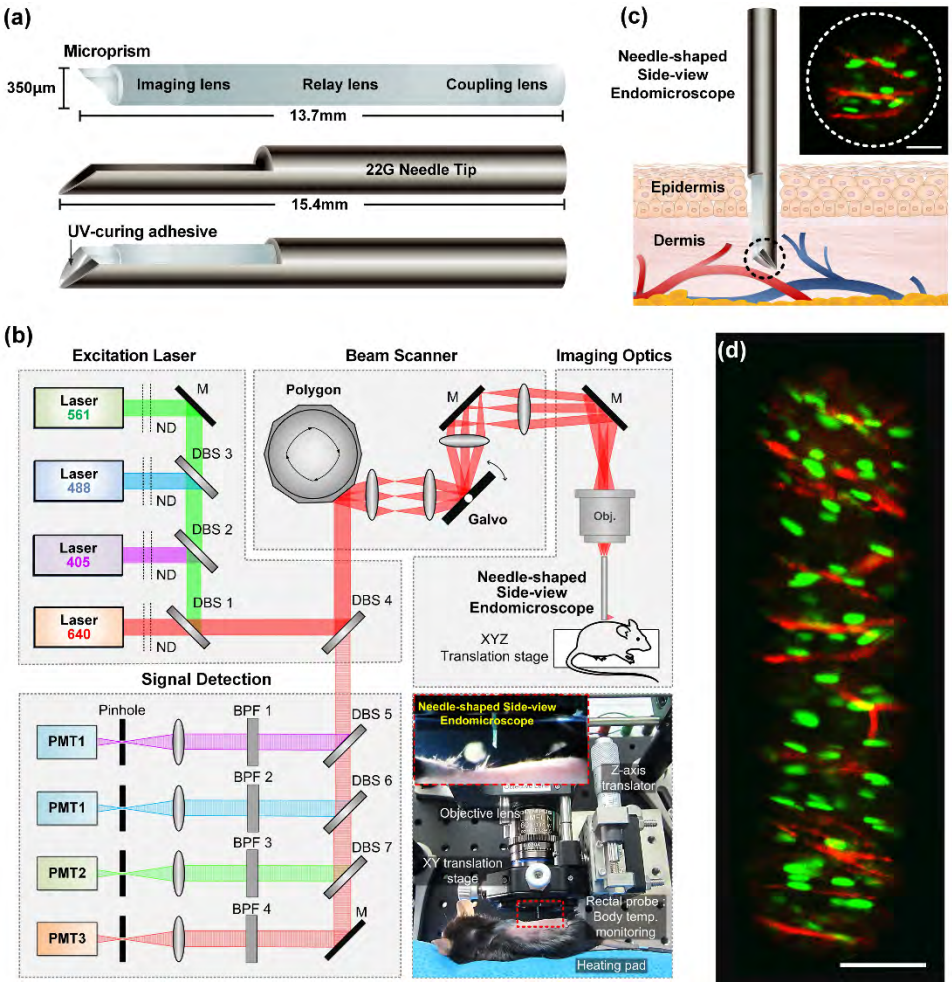

Fig. 1. (a) Schematic of the fabricated needle-shaped side-view endomicroscope packaged into a 22G hypodermal needle tip. (b) Schematic and photo of the custom-built video-rate laser-scanning confocal microscope system and the needle-shaped side-view endomicroscope positioned under the objective lens (M: Mirror, ND: Neutral density filter, DBS: Dichroic beam splitter, BPF: Band pass filter, PMT: Photomultiplier tube). (c) Schematic of the insertion of needle-shaped side-view endomicroscope into the skin to visualize deeper region *in vivo*. The dotted circle presents a representative single FOV image showing nuclei (green) and blood vessels (red) acquired in the dermis. Scale bar: 50 μm. (d) Depth-wise mosaic image constructed by continuously acquired single FOV images during the insertion of the side-view endomicroscope in the mouse dorsal skin. Scale bar: 100 μm.

2.2 Custom-built laser-scanning confocal endomicroscopy

A custom-built video-rate laser-scanning confocal microscope system previously implemented [27,30–32] was used as an imaging system for the needle-type side-view endomicroscope. Figure 1(b) shows a schematic illustration of the custom-built confocal microscope system and photos of the side-view endomicroscope positioned under the objective lens. As excitation sources for multi-color fluorescence imaging, four continuous wave laser modules with output wavelengths of 405, 488, 561, and 640 nm (Coherent OBIS, Cobolt MLD, Cobolt Jive and Cobolt MLD) were used. The excitation lights were combined by dichroic beam splitters (DBS1, FF593-Di03; DBS2, Di01-R405; DBS3, FF520-Di02, Semrock) and then delivered to a multi-edge dichroic beam splitter (DBS4, Di01-

R405/488/561/635, Semrock). 2D laser beam scanning in a raster pattern was achieved by a fast rotating 36 facets polygonal mirror scanner (MC-5, Lincoln Laser) providing 17.28 kHz lateral scanning in the X-axis and a galvanometer mirror scanner (6230H, Cambridge Technology) providing 30 Hz vertical scanning in the Y-axis. The scanning laser beams were then delivered to the back aperture of a commercial objective lens (LUMFLN 60XW, Olympus). The multi-color fluorescence signals from the imaging sample were epi-detected and separated from the excitation laser beams by DBS4. The multi-color fluorescence signals were then split into the single-color signal by dichroic beam splitters (DBS5, FF484-Di01; DBS6, FF560-Di01; DBS7, FF649-Di01, Semrock) and detected by photomultiplier tubes (PMT; R9110, Hamamatsu) through band pass filters (BPF1, FF01-442/46; BPF2, FF02-525/50; BPF3, FF01-600/37; BPF4, FF01-685/40, Semrock). Electronic outputs from the PMTs were digitized by a 4 channel frame grabber (Solios, Matrox) with a sampling rate of 10 MHz. The video-rate images with a frame rate of 30 Hz and a size of 512 × 512 pixels were displayed and recorded in real time by custom-written software using Matrox Imaging Library (MIL9, Matrox).

2.3 Animal model

Mice were housed and bred in an institutional animal facility in Korea Advanced Institute of Science and Technology (KAIST). BALB/c mice were purchased from OrientBio (Suwon, Korea) or bred in-house. Histone H2B-eGFP transgenic mice (Stock no. 006069, Jackson Laboratory [33]), which endogenously express eGFP in nuclei, were used for *in vivo* cellular-level depth-wise visualization from the epidermis to the deeper dermal layer of dorsal skin. For *in vivo* longitudinal and repetitive endomicroscopic depth-wise visualization of tumorigenesis in the single mouse, the breast cancer cells labeled with fluorescence protein, 4T1-Luc2-GFP cells (2.5×10^6), were orthotopically injected into the mammary fat pad of wild-type BALB/c mice. All animal experiments were performed in accordance with the standard guidelines for the care and use of laboratory animals and were approved by the Animal Care and Use Committee of KAIST (protocol no. KA2016-51). All imaging and surgical procedures were performed under anesthesia, and all efforts were made to minimize suffering.

2.4 In vivo imaging procedure

For *in vivo* imaging, the mouse was anesthetized with a mixture of zoletil (30 mg/kg) and xylazine (10 mg/kg) by intraperitoneal injection. Body temperature of the anesthetized mouse was maintained at 36°C by a homeothermic temperature monitoring and control system (RightTemp, Kent Scientific). For the depth-wise visualization of the skin, the skin was shaved by a hair clipper and hair removal cream, and then the side-view endomicroscope was slowly inserted into the dorsal flank. Before the insertion, the target site was cleaned by alcohol swab. For the depth-wise visualization of solid breast tumor tissue, the side-view endomicroscope was gently inserted from the top surface to the bottom of the tumor until it penetrated the whole tumor tissue. For longitudinal observation of tumorigenesis, the growing tumor of the signal mouse was repeatedly imaged from day 9 to day 21 after injection of the cancer cells with 3 day intervals. At each imaging session, the side-view endomicroscope was inserted at the center of the tumor tissue while avoiding the previous insertion site. To simultaneously visualize the microvasculature with the GFP signal in the skin and the tumor, anti-CD31 antibody (Stock no. 553708, BD Biosciences) conjugated with a far-red color fluorophore, AlexaFluor 647 (Stock no. A20006, Invitrogen), was intravenously injected into the mouse at 2 hours before the imaging.

2.5 Preparation of cryosectioned tumor tissue slices

Whole tumor tissues were dissected from the mouse perfused with 4% paraformaldehyde (PFA). Overnight dehydration was carried out twice repeatedly by immersing the tumor tissue

while changing the concentration of PFA to 15% and 30%. The tissue was then placed in a cryomold with optimal cutting temperature compound (OCT compound, Tissue-Tek ™) for freezing. After freezing the tumor tissue filled with OCT, it was sliced using a cryotome machine (FSE Cryostats, Thermo Scientific) to a thickness of 20 μm.

3. Result

3.1 In vivo cellular-level depth-wise visualization of dorsal skin tissue by needle-shaped side-view endomicroscopy

A H2B-eGFP transgenic mouse endogenously expressing eGFP in nuclei was used to demonstrate the depth-wise deep tissue imaging capability of the newly fabricated needle-shaped side-view endomicroscope. As shown in Fig. 1(c), the side-view endomicroscope could be inserted into the dorsal flank skin of an anesthetized H2B-eGFP mouse from the epidermis to the deeper dermis in a minimally invasive manner. In addition to the nuclei expressing eGFP, the microvasculature in the dermis was fluorescently labeled *in vivo* by intravenously injecting anti-CD31 antibody conjugated with a far-red fluorophore at 2 hours before the insertion of the side-view endomicroscope. The dotted circle in Fig. 1(c) shows a representative single FOV image obtained *in vivo* at the deeper dermis in which nuclei of individual stromal cells and capillaries were clearly visible. While inserting the side-view endomicroscope, we could continuously acquire two-color fluorescence images of nuclei and blood vessels at different depths in the skin. To mitigate the chromatic aberration induced focal plane difference between two-color channels, we adjusted the distance between objective lens and surface of coupling lens to sequentially visualize different focal planes by translating only the position of the objective lens. The acquired single FOV images of each channel were projected together then successfully stitched to generate a large-area mosaic image. It shows the depth-wise cellular-level visualization of the skin from the lower epidermis to the deeper dermis, as shown in Fig. 1(d), with a length of 740 μm along the depth-axis at the insertion site.

3.2 In vivo repetitive and longitudinal cellular-level depth-wise visualization of orthotropic breast tumor by needle-shaped side-view endomicroscopy

For the *in vivo* longitudinal depth-wise visualization of tumorigenesis, an orthotopic breast tumor model established by injecting 4T1-Luc2-GFP cancer cells into the mammary fat pad of wild-type BALB/c mice were used. The needle-shaped side-view endomicroscope was repetitively inserted into the growing tumor in a single mouse model from day 9 to day 21 with 3 day intervals after injection of the cancer cells, as depicted in Fig. 2(a). As shown in Fig. 2(b), which presents representative single FOV endomicroscopic images obtained at day 9 and 21, 4T1-Luc2-GFP cancer cells and highly dilated tumor blood vessels in the deep tumor tissue were clearly distinguishable with cellular-level resolution.

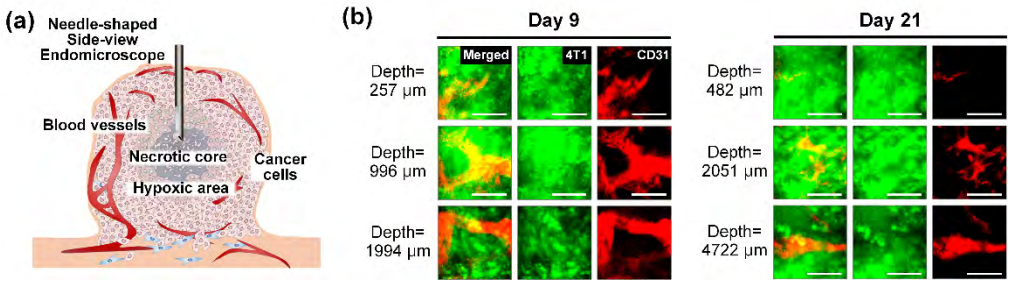

Fig. 2. (a) Schematic of the *in vivo* depth-wise visualization of solid breast tumor tissue with needle-shaped side-view endomicroscope. (b) Representative single FOV endomicroscopic images obtained at various depth in the solid breast tumor at day 9 and 21. Scale bars: 50 μm.

Biomedical Optics EXPRESS

Figure 3 shows depth-wise mosaic images generated by continuously stitching acquired single FOV images obtained from the single mouse at day 9, 12, 15, 18, and 21, respectively. Longitudinal depth-wise visualization from the top to the bottom of the growing tumor was successfully achieved, showing GFP expressing 4T1 breast cancer cells and tumor vessels along the depth-axis. The insertion sites at each repeated insertion of the side-view endomicroscope were carefully selected to penetrate the center of the tumor. The imaged heights of the growing tumor were about 2.1 mm at day 9, 3.6 mm at day 12, 4.1 mm at day 15, 4.7 mm at day 18, and 5.3 mm at day 21, respectively.

3.4 Comparative quantitative analysis of in vivo endomicroscopic tumor images and ex vivo microscopic cryosectioned tumor images

To validate the representativeness of the depth-wise mosaic image obtained by the insertion of the needle-shaped side-view endomicroscope with regard to reflecting the features of the whole tumor tissue, whole tumor tissue dissected from the 4T1 breast cancer mouse models was processed into cryosectioned tissue slices and visualized by a conventional laser-scanning confocal microscope *ex vivo*. Comparative analysis of these cryosectioned whole tumor tissue slice imaging results with the depth-wise endomicroscopic tumor imaging results obtained at the same days (day 9, 12, 15, 18, and 21) after the cancer cell injection was performed.

Figure 4(a) shows a representative *in vivo* endomicroscopic imaging result of the tumor obtained with the needle-shaped side-view endomicroscope at day 9 and a representative *ex vivo* confocal microscopic imaging result of cryosectioned tumor tissue slice dissected on day 9. Figure 4(b-c) present a comparative quantitative analysis of the whole tumor height and the fractional ratio of intra-tumoral vessel area inside the tumor tissue, respectively. As shown in Fig. 4(b), the average tumor heights calculated from the imaging results obtained with two different modalities, *in vivo* side-view endomicroscopy and *ex vivo* confocal microscopy, were similar to each other (n = 4). Although statistically non-significant (t-test) at all of time points from day 9 to day 21, the calculated tumor heights in the cryosectioned tumor tissue slices were slightly smaller, presumably due to the minimal tissue shrinkage induced by dehydration in the process of cryosectioning. Average tumor heights were calculated to be 1.71 ± 0.12 mm in the *in vivo* side-view endomicroscopic imaging group and 1.69 ± 0.04 mm in the *ex vivo* confocal microscopic imaging group at day 9. They continuously increased over time and were calculated to be 5.86 ± 0.54 mm with *in vivo* side-view endomicroscopy and 5.52 ± 0.35 mm with *ex vivo* confocal microscopy, respectively. Additionally, the fractional ratio of the intra-tumoral vessel areas was quantitatively calculated from the imaging results by two modalities using Image J. As was the case with tumor height, the fractional ratios of intra-tumoral vessel areas were also similar in the imaging results of the two modalities (n = 4) with statistical non-significance (t-test), as shown in Fig. 4(c). At day 9, the average fractional ratio of the intra-tumoral vessel area was calculated to be 19.04 ± 1.81% in the *in vivo* side-view endomicroscopic imaging group and 18.25 ± 6.32% in the *ex vivo* confocal microscopic imaging group. Interestingly, subsequently after only 3 days, at day 12, these values were calculated to be significantly decreased to 6.00 ± 1.01% with *in vivo* side-view endomicroscopy and 7.01 ± 0.58% with ex vivo confocal microscopy.

Biomedical Optics EXPRESS

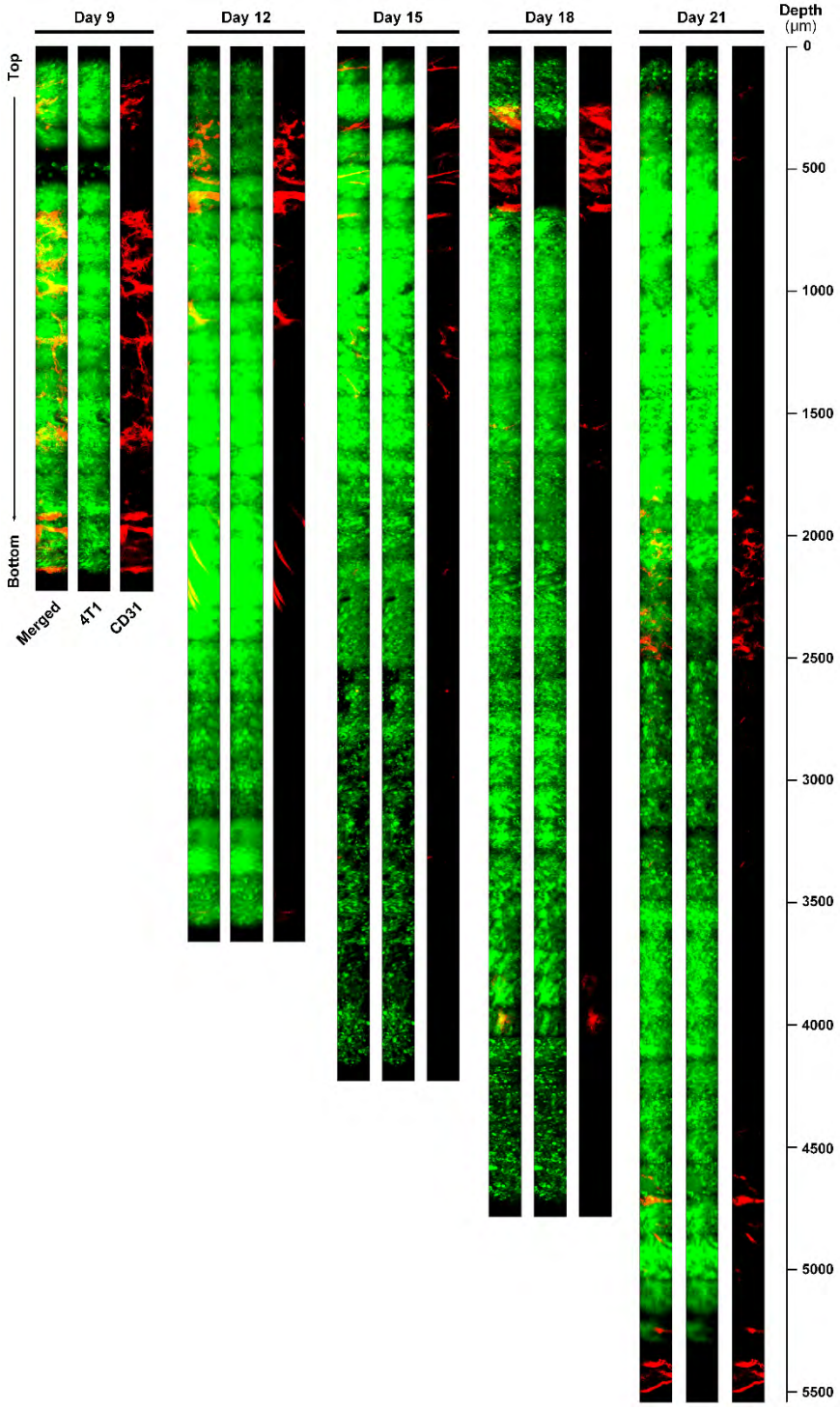

Fig. 3. Depth-wise mosaic images of the growing tumor obtained from a single mouse from day 9 to 21 with 3 day intervals after the inoculation of the cancer cells with continuous insertion of the needle-shaped side-view endomicroscope from the top to the bottom of the breast tumor.

Biomedical Optics EXPRESS

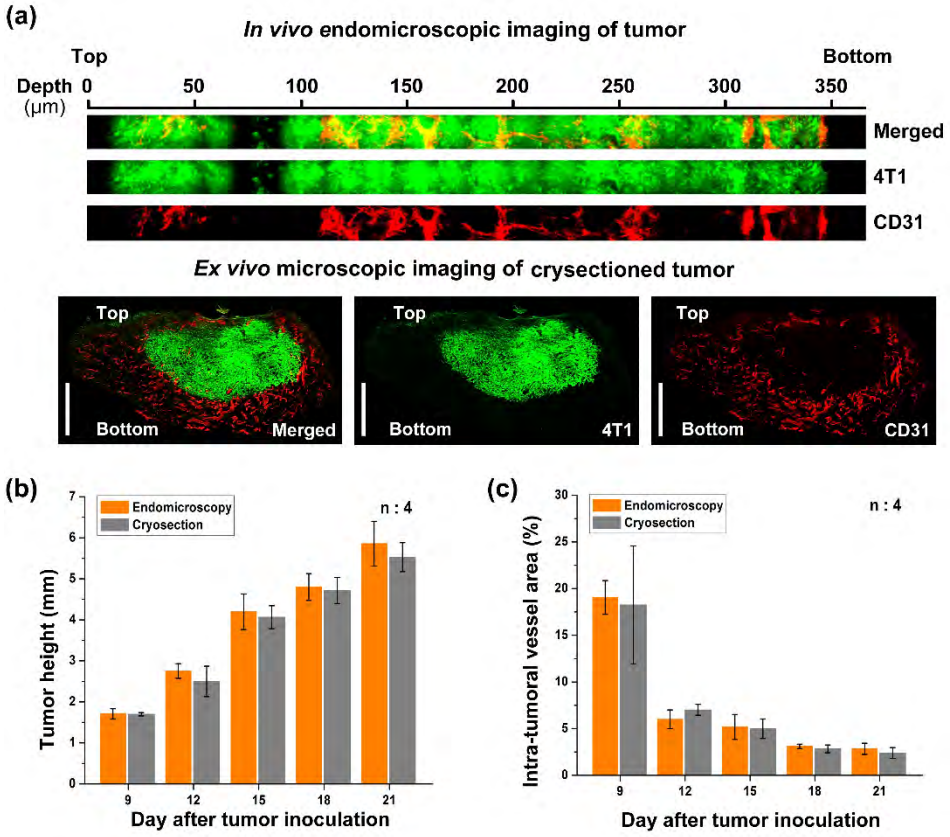

Fig. 4. (a) Representative depth-wise *in vivo* side-view endomicroscopic imaging result of orthotropic breast tumor moue model and conventional *ex vivo* confocal microscopic imaging result of cryosectioned tumor tissue slices dissected from similar mouse model at day 9 after 4T1 cancer cells inoculation. Scale bars: 1 mm. (b, c) Comparative quantitative analysis of whole tumor height and the intra-tumoral vessel area using the side-view needle-type side-view endomicroscopic tumor images and the cryosectioned confocal microscopic tumor images at day 9, 12, 15, 18, and 21.

4. Discussion

To minimize the potential of microvascular damage, insertion sites of needle-shaped endomicroscope were carefully selected not to interfere with vessels visible through the skin over the tumor. The insertion of endomicroscope was performed with small increment of about 100 μm to minimize a sudden physical change to the tissue surrounding the endomicroscope and acquire multi-color fluorescence image at each depth. During the whole insertion and imaging process of the needle-shaped endomicroscope into the tumor, no imaging artifacts those might be caused by the bleeding such as image blurring by fluid, a sudden decrease in imaging brightness, or reduced sharpness were observed. In addition, after the removal of the needle-shaped endomicroscope, no immediate bleeding from the insertion site and no scar formation around the insertion site over time were observed. Based on these observations, collectively, we believe that the damage of microvasculature was minimal although it is still difficult to fully verify or guarantee no damage.

The 4T1-GFP breast tumor grew very rapidly *in vivo* in a relatively short period of time, as shown in Fig. 3 and 4(b). Rapid uncontrolled growth of tumor builds up a unique microenvironment inside the tumor tissue, which is very different from the case of normal tissue. Compared to normal tissue, the solid tumor tissue comprises a highly heterogeneous

extracellular matrix with various growth factors and adhesion molecules, which greatly alters the vasculature inside the tumor [34]. As shown in Fig. 2(b) and Fig. 3, blood vessels observed deep inside the 4T1-GFP breast tumor were greatly dilated and formed a torturous network with excessive branching.

Notably, repeated longitudinal wide-area depth-wise observation of growing tumor through the entire depth by the needle-shaped side-view endomicroscopy revealed a continuous decline of the ratio of intra-tumoral vessel area from day 9 to day 21, as shown in Fig. 4(c). This is because the rapid and exponential proliferation of the 4T1-GFP cancer cells exceeds the speed of angiogenic new blood vessel formation. In addition, the uncontrolled proliferation of 4T1-GFP cancer cells in the center of the tumor compresses the neighboring blood vessels and thereby hampers blood flow. Finally, it is worth noting that the required number of mice to obtain the analysis results shown in Fig. 4(b-c) using the *in vivo* side-view endomicroscopy was five times less than the case with the *ex vivo* confocal microscopy because the single mouse could be repeatedly imaged at each of the five time points between day 9 and day 21.

5. Conclusion

By using a needle-shaped side-view endomicroscope integrated into a laser-scanning confocal microscope, we achieved a depth-wise visualization of microvasculature and tumor cells throughout a solid breast tumor *in vivo*. In a minimally-invasive manner, a repetitive and longitudinal depth-wise visualization of a growing breast tumor in the orthotropic mouse was successfully performed during three weeks, which revealed a decreasing amount of intratumoral blood vessels over the time-course of tumorigenesis. The established method could be a useful tool to image and analyze various cellular-level dynamic changes that occur at the deep center part of a large growing tumor that is normally not accessible by other conventional microscopic imaging methods.

Funding

Global Frontier Project (NRF-2013M3A6A4044716); Basic Research Program (NRF-2017R1E1A1A01074190); and the Bio & Medical Technology Development Program (NRF-2017M3A9E4047243) funded by the Ministry of Science and ICT, Republic of Korea.

Acknowledgments

The authors would like to thank Soo Yun Lee (KAIST) for her technical help on this project.

Disclosures

The authors declare that there are no conflicts of interest related to this article.

References

1. Y. Mao, E. T. Keller, D. H. Garfield, K. Shen, and J. Wang, "Stromal cells in tumor microenvironment and breast cancer," Cancer Metastasis Rev. **32**(1-2), 303–315 (2013).
2. J. A. Joyce and J. W. Pollard, "Microenvironmental regulation of metastasis," Nat. Rev. Cancer **9**(4), 239–252 (2009).
3. T. L. Whiteside, "The tumor microenvironment and its role in promoting tumor growth," Oncogene **27**(45), 5904–5912 (2008).
4. A. Mantovani, T. Schioppa, C. Porta, P. Allavena, and A. Sica, "Role of tumor-associated macrophages in tumor progression and invasion," Cancer Metastasis Rev. **25**(3), 315–322 (2006).
5. A. M. Bode and Z. Dong, "Post-translational modification of p53 in tumorigenesis," Nat. Rev. Cancer **4**(10), 793–805 (2004).
6. G. Bergers and L. E. Benjamin, "Tumorigenesis and the angiogenic switch," Nat. Rev. Cancer **3**(6), 401–410 (2003).
7. R. K. Jain, "Normalizing tumor vasculature with anti-angiogenic therapy: a new paradigm for combination therapy," Nat. Med. **7**(9), 987–989 (2001).
8. S. Lee, H. Jeong, E. Anguluan, and J. G. Kim, "Biphasic tumor oxygenation during respiratory challenge may predict tumor response duringchemotherapy," Curr. Opt. Photon. **2**, 1–6 (2018).

9. R. K. Jain, L. L. Munn, and D. Fukumura, "Dissecting tumour pathophysiology using intravital microscopy," Nat. Rev. Cancer **2**(4), 266–276 (2002).
10. E. Beerling, L. Ritsma, N. Vrisekoop, P. W. B. Derksen, and J. van Rheenen, "Intravital microscopy: new insights into metastasis of tumors," J. Cell Sci. **124**(3), 299–310 (2011).
11. B. J. Vakoc, D. Fukumura, R. K. Jain, and B. E. Bouma, "Cancer imaging by optical coherence tomography: preclinical progress and clinical potential," Nat. Rev. Cancer **12**(5), 363–368 (2012).
12. S. Qi, H. Li, L. Lu, Z. Qi, L. Liu, L. Chen, G. Shen, L. Fu, Q. Luo, and Z. Zhang, "Long-term intravital imaging of the multicolor-coded tumor microenvironment during combination immunotherapy," eLife **5**, e14756 (2016).
13. S. Junankar, G. Shay, J. Jurczyluk, N. Ali, J. Down, N. Pocock, A. Parker, A. Nguyen, S. Sun, B. Kashemirov, C. E. McKenna, P. I. Croucher, A. Swarbrick, K. Weilbaecher, T. G. Phan, and M. J. Rogers, "Real-time intravital imaging establishes tumor-associated macrophages as the extraskeletal target of bisphosphonate action in cancer," Cancer Discov. **5**(1), 35–42 (2015).
14. E. Dondossola, S. Alexander, B. M. Holzapfel, S. Filippini, M. W. Starbuck, R. M. Hoffman, N. Navone, E. M. De-Juan-Pardo, C. J. Logothetis, D. W. Hutmacher, and P. Friedl, "Intravital microscopy of osteolytic progression and therapy response of cancer lesions in the bone," Sci. Transl. Med. **10**(452), eaao5726 (2018).
15. S. W. Yoo, H.-J. Park, G. Oh, S. Hwang, M. Yun, T. Wang, Y.-S. Seo, J.-J. Min, K. H. Kim, E.-S. Kim, Y. L. Kim, and E. Chung, "Non-ablative fractional thulium laser irradiation suppresses early tumor growth," Curr. Opt. Photon. **1**(1), 51–59 (2017).
16. H. A. Lehr, M. Leunig, M. D. Menger, D. Nolte, and K. Messmer, "Dorsal skinfold chamber technique for intravital microscopy in nude mice," Am. J. Pathol. **143**(4), 1055–1062 (1993).
17. G. M. Palmer, A. N. Fontanella, S. Shan, G. Hanna, G. Zhang, C. L. Fraser, and M. W. Dewhirst, "In vivo optical molecular imaging and analysis in mice using dorsal window chamber models applied to hypoxia, vasculature and fluorescent reporters," Nat. Protoc. **6**(9), 1355–1366 (2011).
18. A. Holtmaat, T. Bonhoeffer, D. K. Chow, J. Chuckowree, V. De Paola, S. B. Hofer, M. Hübener, T. Keck, G. Knott, W. C. A. Lee, R. Mostany, T. D. Mrsic-Flogel, E. Nedivi, C. Portera-Cailliau, K. Svoboda, J. T. Trachtenberg, and L. Wilbrecht, "Long-term, high-resolution imaging in the mouse neocortex through a chronic cranial window," Nat. Protoc. **4**(8), 1128–1144 (2009).
19. D. Kedrin, B. Gligorijevic, J. Wyckoff, V. V. Verkhusha, J. Condeelis, J. E. Segall, and J. van Rheenen, "Intravital imaging of metastatic behavior through a mammary imaging window," Nat. Methods **5**(12), 1019–1021 (2008).
20. L. Ritsma, E. J. A. Steller, S. I. J. Ellenbroek, O. Kranenburg, I. H. Borel Rinkes, and J. van Rheenen, "Surgical implantation of an abdominal imaging window for intravital microscopy," Nat. Protoc. **8**(3), 583–594 (2013).
21. L. Ritsma, E. J. A. Steller, E. Beerling, C. J. M. Loomans, A. Zomer, C. Gerlach, N. Vrisekoop, D. Seinstra, L. van Gurp, R. Schäfer, D. A. Raats, A. de Graaff, T. N. Schumacher, E. J. P. de Koning, I. H. B. Rinkes, O. Kranenburg, and J. van Rheenen, "Intravital microscopy through an abdominal imaging window reveals a pre-micrometastasis stage during liver metastasis," Sci. Transl. Med. **4**(158), 158ra145 (2012).
22. R. S. Pillai, D. Lorenser, and D. D. Sampson, "Deep-tissue access with confocal fluorescence microendoscopy through hypodermic needles," Opt. Express **19**(8), 7213–7221 (2011).
23. X. Yang, D. Lorenser, R. A. McLaughlin, R. W. Kirk, M. Edmond, M. C. Simpson, M. D. Grounds, and D. D. Sampson, "Imaging deep skeletal muscle structure using a high-sensitivity ultrathin side-viewing optical coherence tomography needle probe," Biomed. Opt. Express **5**(1), 136–148 (2014).
24. J. K. Kim, J. W. Choi, and S. H. Yun, "350-mu m side-view optical probe for imaging the murine brain in vivo from the cortex to the hypothalamus," J. Biomed. Opt. **18**(5), 050502 (2013).
25. J. K. Kim, J. W. Choi, and S. H. Yun, "Optical fine-needle imaging biopsy of the brain," Biomed. Opt. Express **4**(12), 2846–2854 (2013).
26. Q. Fang, A. Curatolo, P. Wijesinghe, Y. L. Yeow, J. Hamzah, P. B. Noble, K. Karnowski, D. D. Sampson, R. Ganss, J. K. Kim, W. M. Lee, and B. F. Kennedy, "Ultrahigh-resolution optical coherence elastography through a micro-endoscope: towards in vivo imaging of cellular-scale mechanics," Biomed. Opt. Express **8**(11), 5127–5138 (2017).
27. J. Ahn, K. Choe, T. Wang, Y. Hwang, E. Song, K. H. Kim, and P. Kim, "In vivo longitudinal cellular imaging of small intestine by side-view endomicroscopy," Biomed. Opt. Express **6**(10), 3963–3972 (2015).
28. K. Jung, P. Kim, F. Leuschner, R. Gorbatov, J. K. Kim, T. Ueno, M. Nahrendorf, and S. H. Yun, "Endoscopic time-lapse imaging of immune cells in infarcted mouse hearts," Circ. Res. **112**(6), 891–899 (2013).
29. P. Kim, E. Chung, H. Yamashita, K. E. Hung, A. Mizoguchi, R. Kucherlapati, D. Fukumura, R. K. Jain, and S. H. Yun, "In vivo wide-area cellular imaging by side-view endomicroscopy," Nat. Methods **7**(4), 303–305 (2010).
30. I. Park, K. Choe, H. Seo, Y. Hwang, E. Song, J. Ahn, Y. Hwan Jo, and P. Kim, "Intravital imaging of a pulmonary endothelial surface layer in a murine sepsis model," Biomed. Opt. Express **9**(5), 2383–2393 (2018).
31. Y. Hwang, J. Ahn, J. Mun, S. Bae, Y. U. Jeong, N. A. Vinokurov, and P. Kim, "In vivo analysis of THz wave irradiation induced acute inflammatory response in skin by laser-scanning confocal microscopy," Opt. Express **22**(10), 11465–11475 (2014).
32. K. Choe, Y. Hwang, H. Seo, and P. Kim, "In vivo high spatiotemporal resolution visualization of circulating T lymphocytes in high endothelial venules of lymph nodes," J. Biomed. Opt. **18**(3), 036005 (2013).
33. A.-K. Hadjantonakis and V. E. Papaioannou, "Dynamic in vivo imaging and cell tracking using a histone fluorescent protein fusion in mice," BMC Biotechnol. **4**(1), 33 (2004).

Biomedical Optics EXPRESS

34. S. Aznavoorian, M. L. Stracke, H. Krutzsch, E. Schiffmann, and L. A. Liotta, "Signal transduction for chemotaxis and haptotaxis by matrix molecules in tumor cells," J. Cell Biol. **110**(4), 1427–1438 (1990).